Energy 213 (2020) 118789

Contents lists available at ScienceDirect

Energy

journal homepage: www.elsevier.com/locate/energy

Air conditioning system with enthalpy recovery for space heating and air humidification: An experimental and numerical investigation

Peter Niemann*, Gerhard Schmitz

Hamburg University of Technology, Institute of Engineering Thermodynamics, Hamburg, Germany

ARTICLE INFO

Article history:
Received 17 June 2020
Received in revised form
31 August 2020
Accepted 3 September 2020
Available online 9 September 2020

Keywords:
Air conditioning
Desiccant
Enthalpy recovery
System evaluation
System simulation
Modelica

ABSTRACT

This study presents the evaluation of an air conditioning system with enthalpy recovery for space heating and air humidification. Desiccant assisted air conditioning is potentially beneficial against other air conditioning processes in terms of air humidification, counteracting dry indoor air conditions during winter. Furthermore, the overall process can be operated efficiently relying on renewable energy sources. The objective of this work is to investigate a geothermal and desiccant assisted system for different system configurations experimentally and numerically during winter operation. The experimental investigation focuses on differences in system performance for two desiccant materials, lithium chloride and silica gel. Experimental results show that moisture recovery relying on a desiccant wheel with silica gel is beneficial against lithium chloride. An average moisture recovery efficiency of 0.83 was achieved for silica gel. Thermal comfort was maintained on a high level throughout the winter seasons investigated. Based on component and system simulation models, system performance is shown for different boundary conditions during winter requiring space heating and humidification to ensure comfortable indoor air conditions. The simulation results show a reduction in primary energy demand for heat supply by up to 54% by using a high efficient ground-coupled heat pump without backup system.

1. Introduction

Energy-efficient air conditioning is becoming increasingly important due to increasing demands on air conditioning applications worldwide [1]. The International Energy Agency (IEA) estimated an increase of more than five billion air conditioning systems between the years of 2016 and 2050 for the commercial and residential stock [2]. This is more than twice the currently installed units. Income growth in the developing and emerging countries, climate change and increased building energy standards as well as more compact urbanization cause this development [3,4]. Pérez-Lombard et al. [5] reported that heating, cooling, air conditioning and ventilation (HVAC) is responsible for around 50% of buildings' energy demand. Air conditioning systems are primarily used for room air conditioning by providing cooled and dehumidified air. Against the background of required reductions in electrical energy demands for air conditioning applications, desiccant assisted air conditioning is a promising alternative to conventional air conditioning processes relying on vapor compression chillers. For this reason, numerous studies have been carried out to investigate and improve both the hygroscopic materials and various system configurations [6–8]. Although winter operation is an essential part of full-year operation, especially in regions dominated by heating loads, heating mode and full-year operation have so far only been considered in a few studies. Within a desiccant assisted system, moisture recovery based on the already existing hygroscopic material is possible. This enables the humidity of supply air to be increased without additional required components as part of the air handling unit.

In De Antonellis et al. [9] humidification of supply air was investigated experimentally on the basis of a desiccant wheel with silica gel for Mediterranean winter conditions. For their optimal configuration a moisture uptake of 3.2 g_w/kg_{air} at an outside air temperature of 10 °C was obtained. A comparison with conventional air humidifiers showed benefits of using a desiccant wheel for air humidification against an electrical steam humidifier in terms of primary energy demand. La et al. [10] analyzed a solar driven system with one-rotor two-stage desiccant wheel for winter operation in Shanghai, both experimentally and numerically. The system proposed uses extract air from the air conditioned space to

* Corresponding author. Hamburg University of Technology, Hamburg, Germany.
E-mail addresses: peter.niemann@tuhh.de (P. Niemann), schmitz@tuhh.de (G. Schmitz).

https://doi.org/10.1016/j.energy.2020.118789

humidify supply air preheated with solar energy. The study revealed a significant increase of thermal comfort due to air humidification. The solar coverage of the heat supply was obtained in the range of 30%–60%. Kawamoto et al. [11] presented the investigation of a desiccant assisted system in combination with a heat pump to provide thermal energy on the regeneration airside for a few winter days in eastern Japan. Using an active dehumidification process, a minimum humidity ratio of the supply air of 5.8 g_w/kg_{air} was achieved at a regeneration air temperature of 50 °C. Kashif et al. [12] experimentally analyzed a solar and desiccant assisted air conditioning system with silica gel during winter in Pakistan. They found an average moisture recovery efficiency of 0.74. An electrical heater was used as the backup system which caused a significant impact on the system's performance. Thermal comfort was achieved throughout the considered winter period with a humidification effectiveness in the range of 0.66–0.82. Preisler and Brychta [13] experimentally investigated full-year operation for a desiccant evaporative system in Austria. Heating was provided by a solar thermal system in combination with a gas boiler. During full-year operation, primary energy demand was reduced by 60% compared with an equivalent air conditioning system relying on a vapor compression chiller. Further explanations on the investigation of desiccant assisted air conditioning in winter and full-year operation can be found in Niemann and Schmitz [14] just as Niemann et al. [15].

Increasing the humidity level of supply air is not a negligible aspect in terms of human comfort and health. Dry indoor air conditions in air-conditioned buildings without additional humidifiers in winter can affect comfort and health of people [16,17]. Noti et al. [18] examined the probability of survival of influenza virus at different humidity ratios of indoor air and found a significant decrease in infectivity at humidity ratios above 40 % RH. In addition, the importance of operating air conditioning systems that are harmless to health is increasing. In this context, the operation of a desiccant assisted system can be advantageous [19]. The antibacterial and germicidal effect of lithium chloride as the desiccant material used favors a high degree of hygiene in the supply air without additional air treatment processes. Li and Li [20] investigated air cleaning effects of a desiccant wheel with silica gel. The authors found promising air cleaning effects for this desiccant but further details are not provided.

With the present publication the authors want to contribute to the investigation of air conditioning systems with moisture recovery and the use of environmental energy against the background of cold and dry outside air conditions. The system on which this study is based has proven to be a promising alternative to conventional air conditioning systems for temperate climates [15]. Furthermore, Speerforck [21] showed the applicability of the system for different locations during summer using a dynamic system simulation model. In the present study, the proposed system is investigated for winter operation. Different air humidification processes are compared in order to show the strengths and weaknesses of desiccant materials used for moisture recovery. In addition to the previous investigations in Ref. [14], heating and air humidification are investigated for different boundary conditions, both experimentally and numerically.

2. Test facility

The investigated test facility, operated on the campus of Hamburg University of Technology since 2012, is already described in Refs. [14,15] for winter and full-year operation. Thus, the following system description is limited to essential characteristics and required information regarding the present study.

2.1. System layout

Getting into the details of the investigated system, Fig. 1 shows the schematic layout that can be divided into the following subsystems: reference room, air handling unit and hydraulic circuits. Designed as a hybrid system, the test facility combines an open desiccant assisted enthalpy recovery process with a closed-loop heating circuit during winter. The air handling unit (AHU) is designed as a two-wheel system relying on a heat recovery wheel (HRW) and a desiccant wheel, operated in enthalpy recovery mode (EW). The reference room is equipped with different thermally activated building systems for sensible heat transfer. Underfloor heating (UH) as well as ceiling heating (CH) are investigated in this study.

A brief description of the air state changes during winter operation is provided below. The relevant information are also summarized in Table 1.

In enthalpy recovery mode (dark gray path), outside air (oda) is passed through a desiccant wheel, operated as enthalpy exchanger (1 → 2). During this state change there is a combined heat and mass transfer to the process air side. If necessary, the air temperature is increased to the set point of supply air (sup) in a water-to-air heat exchanger (3 → 4), before it is fed to the reference room. If the outside air is already with in the required comfort range with regard to the humidity ratio, the process air is preheated by means of the heat recovery system (2 → 3), before it is adjusted to the desired value of ϑ_{sup} passing the reheater. In this case the EW is bypassed (light gray path). The extract air (exa) from the room is used either for sensible heat transfer at the HRW (5 → 6) or for the coupled heat and mass transfer at the EW (7 → 8), before it is released to the environment. A heater (6 → 7) can be used to increase ϑ_{exa} in order to avoid condensation in the EW at very low values of ϑ_{oda}. A stationary operation state during EW mode is shown in the psychrometric chart in Fig. 2. The state changes are marked according to Fig. 1. Since there are almost no state changes across the fans, the corresponding air conditions downstream the fans are not plotted. In order to keep the plot clear, the measurement uncertainties of the stationary states are not included.

Energy is provided in the form of heat during the heating season, primarily by a ground-coupled heat pump (GCHP). A gas driven micro cogeneration unit, combined heating and power generation (CHP), is used as the backup system and to cover peak loads throughout the year. Furthermore, a solar thermal unit (STU) is integrated as the primary heat source for summer operation within the hot water circuit of the system and is also used as a subordinate heat source in winter operation. All heat supplying systems are connected to a stratified thermal storage system with a capacity of1 m^3 Technical details of heat supplying systems are summarized in Table 2.

The geothermal system is based on two identical geothermal probes with a final drilling depth of 80 m, as shown in Fig. 3. These are designed as double U-tube borehole heat exchangers (BHE). A single BHE (BHE 2) is used to operate the system, whereas the second geothermal probe (BHE 1) is used as the reference BHE to investigate the thermal effects on the surrounding soil. In both systems, a thermistor string is installed for discretized temperature measurement within the grouting material at different depths. The soil at the drilling location is mainly characterized by micaceous clay below 30 m, while sand is predominant in the layers of soil above. There is no significant flow of groundwater, so that the soil can be characterized as a seasonal thermal energy storage.

The reference room is set up of four 20 ft containers. These are built as an office and meeting room with an effective area of $A = 54$ m^2 and designed as a single building area. Parts of the room layout are shown in Fig. 4. The heat transition coefficient of the

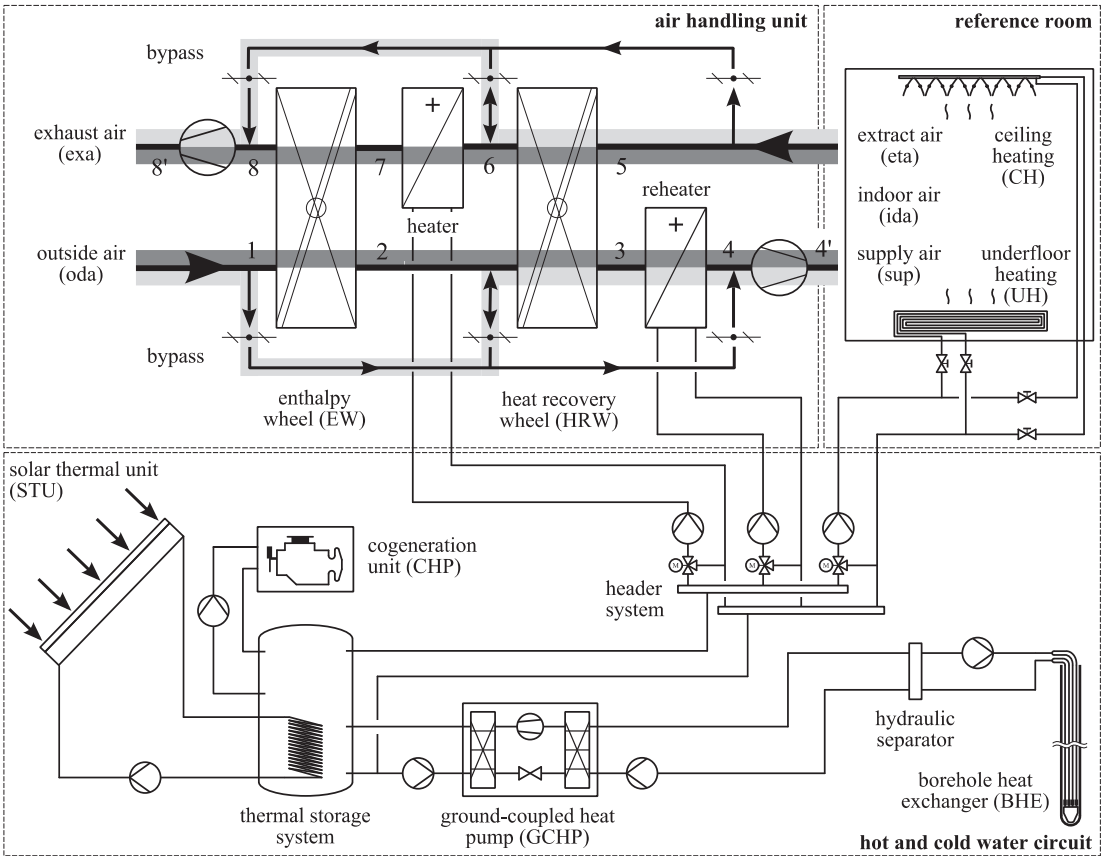

Fig. 1. Simplified system layout of the test facility used during winter operation.

Table 1
Air state changes within the AHU depending on operation modes.

State change	EW mode	HRW mode
1 → 2	Enthalpy transfer	Bypass
2 → 3	- (HRW not used)	Sensible heat transfer
3 → 4	Sensible heat transfer	Sensible heat transfer
5 → 6	- (HRW not used)	Sensible heat transfer
6 → 7	- (heater not used)	Bypass
7 → 8	Enthalpy transfer	Bypass

Table 2
Technical details of heat supplying systems.

System	Specification
GCHP	reciprocating compressor $\dot{Q}_{GCHP,max} = 5.1\ kW_{th}$ at BW5/W30
CHP	Gas engine $\dot{Q}_{CHP,max} = 12.5\ kW_{th}$, $P_{CHP,max} = 5\ kW_{el}$
STU	Flat plate collectors $\dot{Q}_{STU,max} = 7.5\ kW_{th}$, $A_{STU} = 20\ m^2$

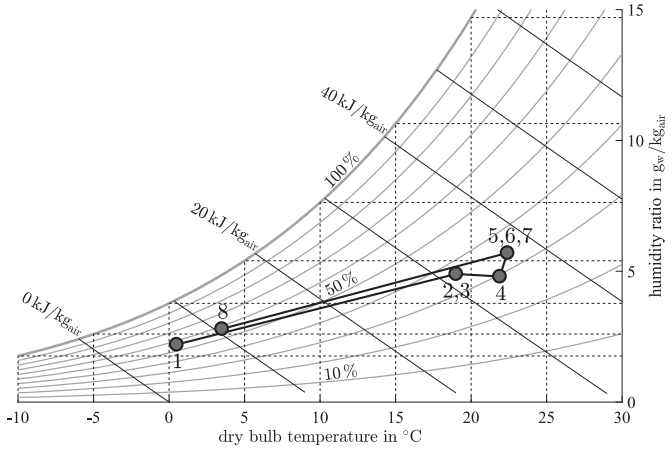

Fig. 2. State changes of air in the air conditioning process during steady state in EW mode.

walls is $k = 0.33 W/(m^2K)$.

2.2. Operation strategy

For the investigated heating seasons in 2017 and 2018, the overall process was operated with different system configurations regarding moisture recovery and heat supply. Even though a bivalent and partially parallel operation of the ground-coupled heat pump and the cogeneration unit was undertaken in combination with the solar thermal unit during both periods, the operation of heat supply and the interaction of GCHP and CHP differed. This holds also true for the desiccant material and the space heating devices. For 2018, the GCHP was partially operated during night to improve thermal comfort in the morning. To analyze the influence of the air exchange rate on thermal energy demand and moisture recovery, the volumetric flow rates were reduced by 26% for plant operation in 2018 compared with the previous heating period. Investigations on silica gel showed increased moisture recovery performance in the range of $8 - 12$ % for the lower volumetric flow

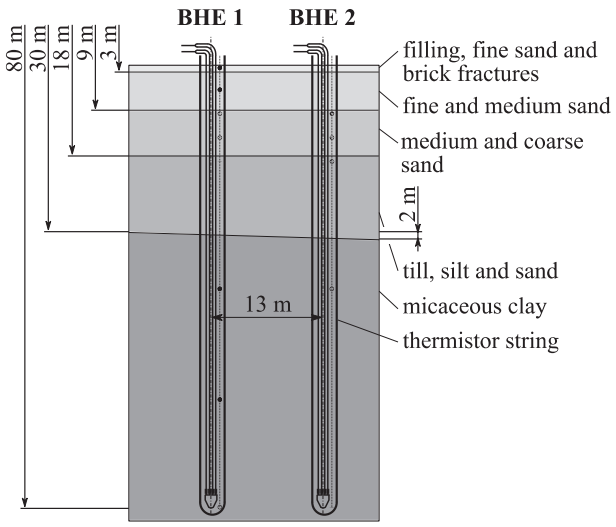

Fig. 3. Geology and structure of the geothermal system.

rate. Lithium chloride was not tested for lower volumetric flow rates. The main characteristics of plant operation during both winter seasons are summarized in Table 3.

Table 4 lists the ratio of EW and HRW operation times for both periods. With the given outside air conditions, moisture recovery was required for additional 19% in 2018 compared with the previous season.

2.3. Metrological equipment

The measurement data acquisition of the overall system comprises around 350 measuring points. A brief description relevant for this study is provided below. Air temperature and relative humidity are measured before and after each component of the AHU, and the pressure loss across each component is also recorded. The volumetric flow rates $\dot{V}_{sup}$ and $\dot{V}_{exa}$ are measured indirectly at the fans based on the effective pressure method. In each circuit of the hot and cold water system, the volumetric flow rate of the heat transfer medium and the temperature at the inlet and outlet of the corresponding component are measured. The temperature in the

Table 3
Specific characteristics of plant operation for the winter seasons investigated.

Parameter	2017	2018
Period	January till March	January till March
Heat supply	GCHP, CHP, (STU)	GCHP, CHP, (STU)
Desiccant	Lithium chloride (LiCl)	Silica gel (SiO_2)
Space heating	UH (dry construction)	CH (convection bars)
Night time operation	UH	CH, GCHP
Volumetric flow rate	$\dot{V}_{sup} = (950 \pm 95)\ m^3/h$	$\dot{V}_{sup} = (700 \pm 70)\ m^3/h$

Table 4
Ratio of operation times.

Wheel	2017	2018
EW	70%	89%
HRW	30%	11%

grouting material of each borehole heat exchanger is determined by means of a thermistor string. All measurement signals are recorded with an interval of 1 min. Most sensors were calibrated on site and an annual recalibration is carried out for the humidity sensors due to principle-related drift phenomena. Relevant characteristics in terms of measurement devices and related measurement uncertainties are summarized in Table 5. A comfort measurement setup was used to evaluate thermal comfort in detail according to DIN EN ISO 7726 [22] and DIN EN ISO 7730 [23]. The test rig was installed within the reference room as shown in Fig. 4. According to Ref. [22], air and globe temperature were measured in four different heights above the floor (0.1, 0.6, 1.1 and 1.7 m). Globe temperature was measured using thin-walled hollow spheres in matt black color ($d = 145$ mm). Sensors measuring air temperature were radiation protected. Relative humidity and air velocity were measured at one location each. Additionally, floor surface temperature was measured at four different positions as shown in Fig. 4(b). Measurement devices and related measurement uncertainties for the comfort measurement setup are also listed in Table 5. A standalone controller is used is used to record measurement signals once per minute.

Generally, cooling and dehumidification of process air were not provided during winter operation. Data acquisition design and system control strategy as well as error analysis of experimental results is equal to the explanations in Ref. [15].

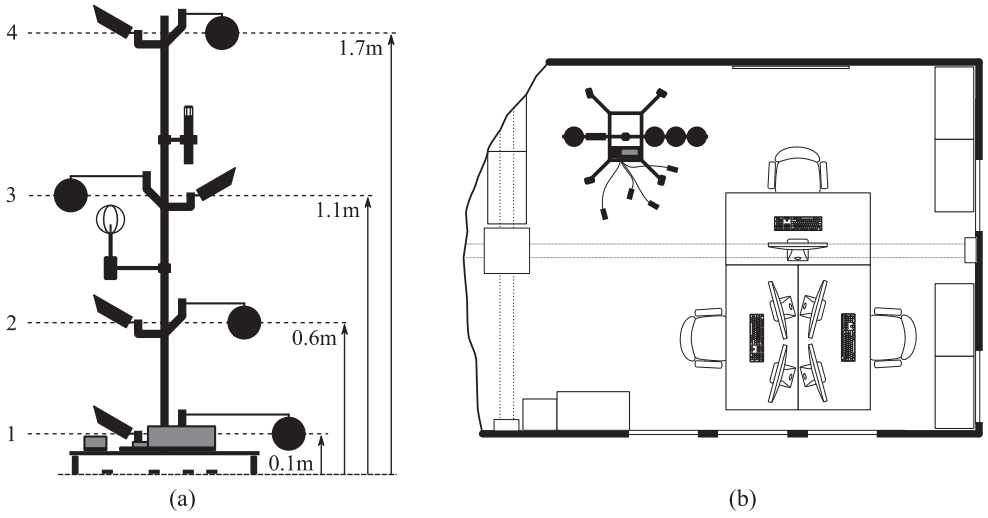

Fig. 4. Design (a) and installation (b) of the comfort measurement setup within the reference room.

Table 5
Measurement devices used and related measurement uncertainties.

Measured value		Sensor type/measuring principle	Measurement uncertainty
Test facility			
Air and water temperature	ϑ	Pt100 (accuracy class W 0.1)	$\pm 1/3 \cdot (0.3 + 0.005 \cdot \vartheta)$ K
Soil temperature	ϑ	Thermistor string	$\pm$ 0.5 K
Relative humidity	ϕ	Capacitive humidity sensor	$\pm$ 2 % RH for 10 – 90 % RH
Volumetric flow rate (air)	$\dot{V}$	Differential pressure	$\pm$ 10 % of reading
Volumetric flow rate (water)	$\dot{V}$	Electromagnetic flow meter	$\pm$ 0.5 % of reading $\pm$1 mm s^{-1}
Pressure difference	$\triangle p$	Ceramic fulcrum lever technology	$\pm$ 2 % of full scale (range: 0 – 300 Pa and 0 – 1000 Pa)
Electric power	P	AC energy meter	$\pm$ 2 % of reading
Comfort measurement setup			
Air and globe temperature	ϑ	Pt100 (accuracy class F 0.1)	$\pm 1/3 \cdot (0.3 + 0.005 \cdot \vartheta)$ K
Floor surface temperature	ϑ	Pt100 (accuracy class F 0.15)	$\pm (0.15 + 0.002 \cdot \vartheta)$ K
Relative humidity	ϕ	Capacitive humidity sensor	$\pm$ 2 % RH for 10 – 90 % RH
Air velocity	v_a	Hot-wire anemometer, omnidirect	$\pm$ 1.5 % of reading

3. Experimental investigation

Experimental results presented in this study are based on measured data of the periods considered. Full system operation was provided from 7 a.m. to 10 p.m. every day of the week, whereas only some subsystems were operated up to 24 h a day for heat supply and distribution. Daily occupancy was essentially limited to the period from 8 a.m. to 9 p.m. Moisture loads inside the reference room were similar for both seasons. The release of water vapor by people was almost constant at 0.61kg$_w$/h during working weeks and 0.38kg$_w$/h at the weekends. This corresponds to a constant occupancy of approx. 12 (working weeks) or 6 (weekends) persons, simulated by humidifiers within the reference room in addition to the people present. Weather conditions in the form of ϑ_{oda} and x_{oda} are provided in Fig. 5 for the periods investigated. Even though the number of heating days (term: $\bar{\vartheta}_{d,oda} < 15$ °C), according to the German Weather Service, was similar for both periods, the number of frost days (term: $\vartheta_{d,oda,min} < 0$ °C) was twice as high for 2018 compared with 2017 (2017: 20, 2018: 40).

The following system evaluation and performance analysis is divided into three parts. First, air treatment and enthalpy recovery are evaluated. The second part follows up with the consideration of heat provision and distribution. Finally, thermal comfort within the reference room and limitations of thermal comfort are evaluated.

3.1. Air treatment and enthalpy recovery

During both periods, the rotational speeds of EW and HRW were kept constant. The optimal rotational speed of both EW and the HRW were specified in previous investigations that are $\omega_{EW,LiCl} = \omega_{HRW} = 248$ rph and $\omega_{EW,SiO_2} = 237$ rph. Passive enthalpy transfer was realized during winter in contrast to active air dehumidification in summer mode using a regeneration air heater, see Fig. 1. Thus, the moisture recovery efficiency Ψ can be defined equivalent to the key figure of heat recovery efficiency, see Equations (1) and (2). The numbers are according to Fig. 1.

$$\Psi = \frac{\Delta x_{pro}}{\Delta x_{max}} = \frac{x_{pro} - x_{oda}}{x_{eta} - x_{oda}} = \frac{x_2 - x_1}{x_7 - x_1} \tag{1}$$

The heat recovery efficiency is defined as shown in Equation (2).

$$\Phi = \frac{\Delta \vartheta_{pro}}{\Delta \vartheta_{max}} = \frac{\vartheta_{pro} - \vartheta_{oda}}{\vartheta_{eta} - \vartheta_{oda}} \tag{2}$$

Figures shown in the following rely on steady-state conditions. Measured data were taken into account for steady-state operation if fluctuations in humidity ratio and temperature were $\Delta x_{sup} < \pm 0.5 g_w/kg_{air}$ and $\Delta \vartheta_{eta} < \pm 0.5$ °C within 15 min. Fig. 6 shows the key value of moisture recovery efficiency according to Equation (1) and the increase of x_{sup} in dependence of the given moisture potential Δx_{max}.

Comparing both materials shows some similarities as well as performance differences. Generally, a slight increase in moisture recovery efficiency with increasing moisture potential is visible for both materials. The slopes of the resulting linear trends are $\Delta\Psi < 0.05/(g_w/kg_{air})$ in both cases. This dependence was much

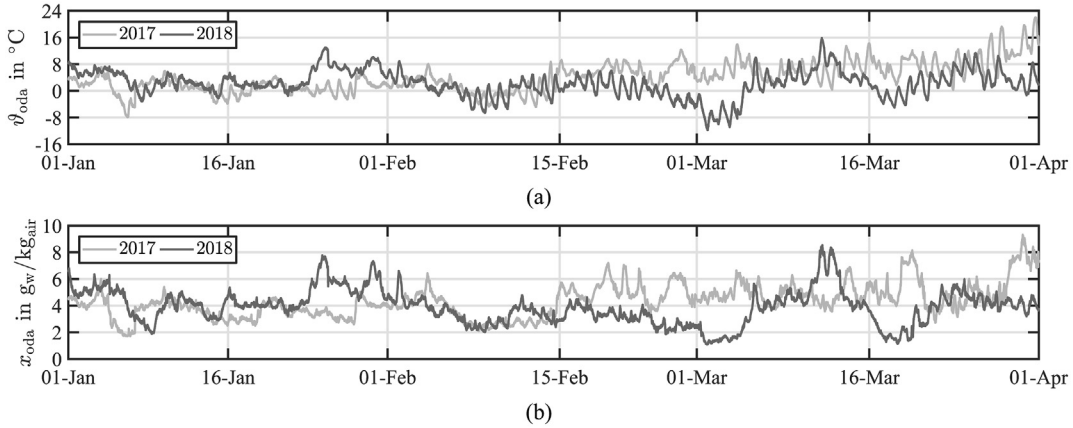

Fig. 5. Outside air temperature (a) and humidity ratio (b) throughout the periods investigated.

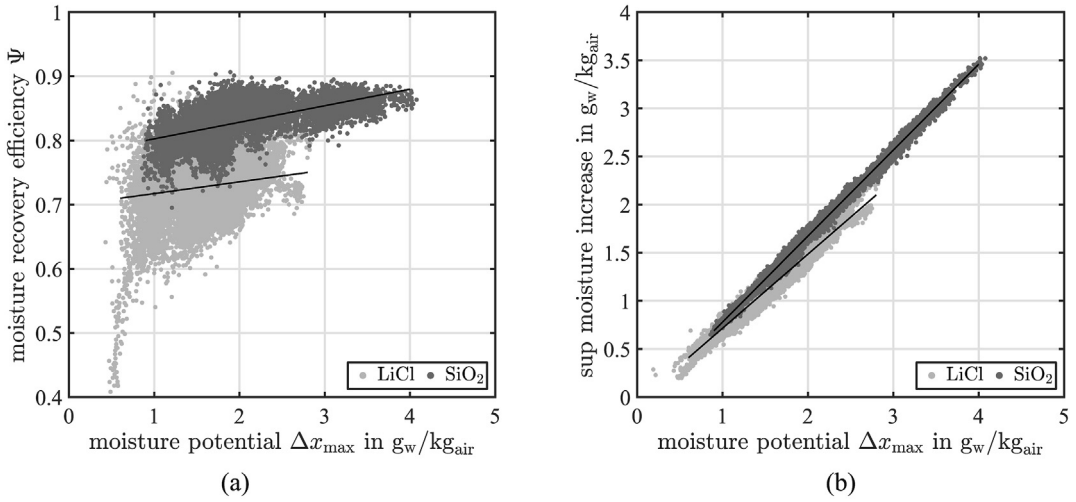

Fig. 6. Performance of moisture recovery by means of moisture recovery efficiency (a) and total moisture recovery (b) for the desiccant materials investigated.

less fluctuating for SiO_2 compared with LiCl. The range of Δx_{max} was increased by around $1.5 g_w/kg_{air}$ for SiO_2, matching the average moisture potential for LiCl properly. Values of Ψ were generally 10% higher for SiO_2 at comparable values of Δx_{max}. The resulting average moisture recovery efficiencies are $\overline{\Psi}_{LiCl} = 0.75$ and $\overline{\Psi}_{SiO_2} = 0.83$. Due to the low dependence of Ψ on Δx_{max}, total moisture increase Δx_{pro} results as a linear function of Δx_{max} for both materials as shown in Fig. 4(b). Due to higher values of Ψ_{SiO_2}, the linear trend is steeper for SiO_2. Thus, the resulting increase of $\overline{x}_{sup}$ was $1.1 g_w/kg_{air}$ using LiCl and $1.7 g_w/kg_{air}$ using SiO_2, respectively. Regarding sensible heat transfer at the EW, average heat recovery efficiencies of $\overline{\Phi}_{LiCl} = 0.7$ and $\overline{\Phi}_{SiO_2} = 0.89$ were obtained. Summarizing, the investigations show high efficiency of heat and mass transfer at the EW. Numerical investigations of different desiccant materials, LiCl and SiO_2 among others, approved best heat and moisture recovery for SiO_2 for most of the operating points examined. These simulations were based on physical and validated models using the Modelica modeling language. The results of numerical investigations of the system are presented in Section 4. Reasons for better enthalpy transfer performance can be found in the specific material properties. Even though the sorption capacity of LiCl is twice as high as that of SiO_2, as a chemical sorbent it performs poorly in heat and mass transfer due to large volume expansion and agglomeration. The ratio of sensible and latent heat transfer is 4:1 for both EW. Thus, enthalpy transfer is mostly characterized by sensible heat transfer. For the HRW, an average heat recovery efficiency of $\Phi_{HRW} = 0.83$ was assessed during both periods.

In order to further evaluate the performance of the air handling process relying on LiCl or SiO_2, specific periods with similar values of ϑ_{oda} and x_{oda} are considered. Figs. 7 and 8 show the outside and indoor air conditions as well as the reheating demand for selected periods that were characterized by low values of ϑ_{oda} and x_{oda} with respect to Köppen-Geiger climate classification *Cfb* [24]. Gray shading marks periods during system operation.

The trajectories of x_{oda} and x_{sup} confirm a higher moisture recovery performance of SiO_2 compared with LiCl. As a result, the desired limit x_{lim} was not achieved with LiCl, whereas this requirement was met using SiO_2, at least during workdays. Due to lower internal moisture loads of the room at the weekends, it was not possible to sufficiently humidify process air even with SiO_2. With respect to heat recovery, the significantly increased efficiency when operating with SiO_2 is evident from the required thermal output of the reheater; an average reduction to a quarter was determined. Another difference can be observed for the course of ϑ_{room}. The reason for the more uniform temperature level in 2018 is the quick responding characteristic of the CH due to the small masses that have to be heated in contrast with the multi-layer floor construction.

3.2. Heat provision and distribution

The GCHP system was operated in modulating mode at primarily two power levels at 60% and 100%. These power levels were controlled according to the required heat flux for space heating and the reheater. The objective of this control strategy was to run the GCHP at the maximum coefficient of performance for most operating points. The GCHP showed poor operation conditions at required high supply temperatures of UH or CH and in parallel operation with the CHP. The significantly higher temperature level of supply temperature to the thermal storage system comes along with increased condenser inlet temperature and required GCHP temperature lift. The total range of GCHP performance was limited to $COP_{GCHP} = 2.8 - 3.9$. The corresponding definition of COP_{GCHP} is provided in Equation (3).

$$COP_{GCHP} = \frac{\dot{Q}_h}{P_{GCHP} + P_{AUX}} \tag{3}$$

Fig. 9 shows the average daily thermal energy supply (a) and demand (b).

The average daily thermal energy supply was distributed similarly for both seasons with a total deviation of 4.6%. However, the additional share of night time GCHP operation has to be taken into account for 2018. Even though the average daily thermal energy demand was quite identical, thermal energy distribution shows significant differences for the seasons considered. This holds especially true for the amount of thermal energy that was required for reheating and daytime space heating. First, thermal energy demand for reheating was reduced by 76.1% for 2018 as an effect of improved heat recovery within the AHU. An opposite trend is visible for the space heating demand. Due to the lower heat capacity of the ceiling heat exchanger, increased effects of ventilation heat losses and lower $\overline{\vartheta}_{oda}$, daytime space heating demand was increased by 37.8% in 2018. Summarizing, decreased thermal

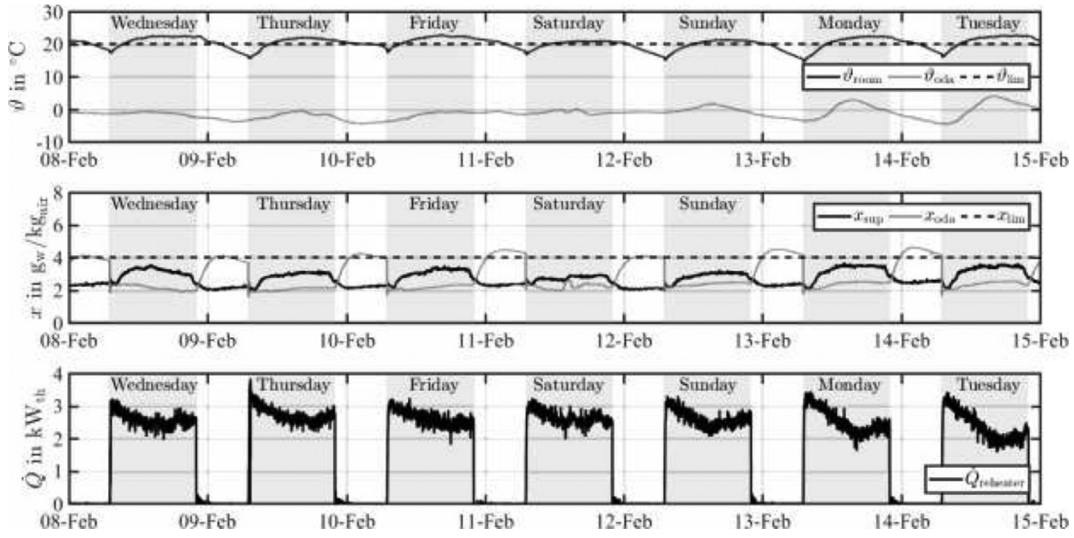

Fig. 7. Outside and indoor air conditions (top and center) as well as reheating demand (bottom) for a period at low values of ϑ_{oda} and x_{oda} using LiCl (February 8th to 15th, 2017).

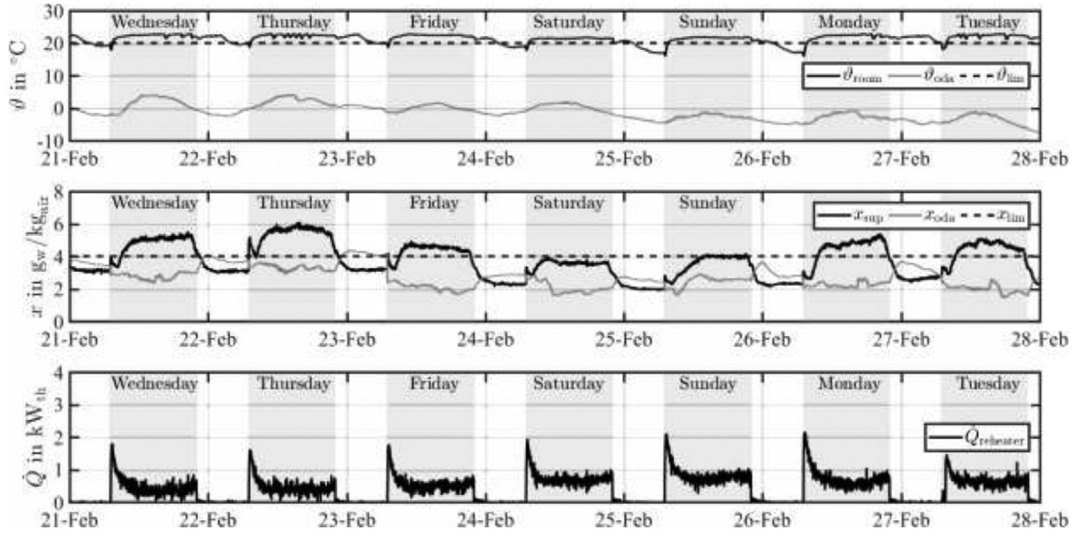

Fig. 8. Outside and indoor air conditions (top and center) and reheating demand (bottom) for a period at low values of ϑ_{oda} and x_{oda} using SiO_2 (February 21st to 28th, 2018).

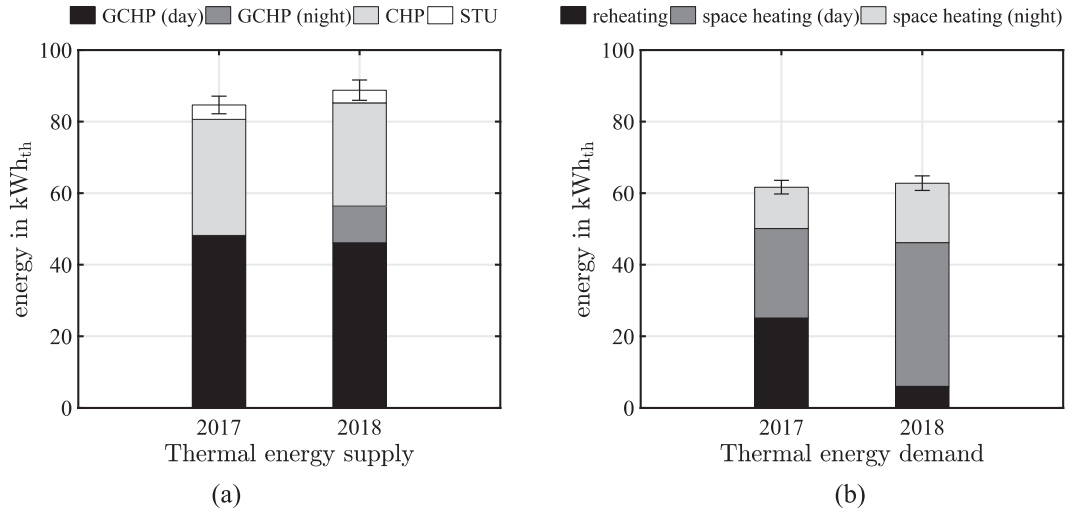

Fig. 9. Average daily thermal energy supply (a) and demand (b), separated by supplying and distributing systems for the investigated heating seasons.

energy demand for reheating was substituted by additional required thermal energy demand for space heating in 2018.

To further analyze the composition of heat supply, the GCHP cover ratio α_{GCHP} was used as presented in Equation (4).

$$\alpha_{GCHP} = \frac{\int \dot{Q}_{GCHP}\, d\tau}{\int (\dot{Q}_{GCHP} + \dot{Q}_{CHP} + \dot{Q}_{STU}) d\tau} \quad (4)$$

with respect to the control strategies implemented, a GCHP cover ratio of $\alpha_{GCHP,2017} = 0.57$ was achieved in 2017 and it was increased to $\alpha_{GCHP,2018} = 0.64$ in 2018. The remaining cover ratio was primarily assigned to the CHP, whereas the STU cover ratio was less than 5% for both periods. The additional required electrical energy demand to run the GCHP at night has to be taken into account as direct effect on improved thermal comfort within the reference room of the test facility.

3.3. Thermal comfort

The resulting level of thermal comfort was comparable for both periods as shown in Fig. 10. Indoor air conditions were evaluated based on the comfort criteria given by the German standard DIN EN 15251 [25], divided into different comfort categories (cat.). Indoor air conditions according to cat. I (< 6 % of dissatisfied occupants) and cat. II (< 10 % of dissatisfied occupants) were maintained for 21 %/93 % (2017) and 22 %/88 % (2018) of operation time during the analyzed periods. Furthermore, an indoor clothing insulation of $I_{cl} = 0.8$ clo (including insulation of the office chair) was assumed with respect to winter outside conditions. Equalizing the operation strategy for UH and CH caused decreased thermal comfort using CH for space heating due to its operating principle against the natural heat convection in general. This aspect is further discussed below. The remaining violations of cat. I/II were almost exclusively due to the low indoor air humidity ratio in 2018. This was justified with insufficient x_{sup} and insufficient internal moisture loads of the room. In contrast, low indoor air temperatures were the main reason for uncomfortable indoor air conditions in 2017. Such conditions occurred primarily in the first hours after starting the system, violating the requirements of cat. I/II for 24–33% from 8 a.m. to 10 a.m. during both periods as shown in the right plots of Fig. 10(a) and (b). Summarizing, the results represent a high level of thermal comfort within the reference room due to surface heating and enthalpy recovery.

In order to further analyze restrictions on thermal comfort, the space heating systems are examined with regard to ϑ_{ida}, as this has a significant influence on thermal comfort. The operation strategy of underfloor and ceiling heating was relying on a standard heating curve using the current value of ϑ_{oda}. With regard to Fig. 11, a trend of increasing fluctuation of ϑ_{room} with increasing inlet temperature of the space heating system is noticeable. These fluctuations are more evident when using underfloor heating, as the GCHP system was not used for overnight heating. Another effect can be attributed to the positioning of the sensor for ϑ_{room} used to control the space heating systems, which was installed at a height of 2 m above the floor and is therefore close to the ceiling. Operation states with lower ϑ_{room} than the set point temperature ($\vartheta_{room,set} = 22$ °C) at $\vartheta_{in,UH} > 35$ °C just occurred during the first hours after system start-up, limiting thermal comfort in the morning as mentioned above.

(a) Space heating with underfloor heating, winter 2017 (b) Space heating with ceiling heating, winter 2018.

With the help of the comfort measurement setup the impacts of the space heating systems on local thermal comfort were further examined, according to the method presented in Ref. [22]. Fig. 12 shows air temperatures at different heights above the floor (a) as well as local thermal discomfort in terms of vertical temperature differences and warm or cold floor (b).

As shown in Fig. 12(a), the differences in average temperature distribution using underfloor or ceiling heating are clearly visible. When using underfloor heating, the time and height averaged temperature was about 1 K higher and at the same time the vertical temperature stratification was much more homogeneous compared with the ceiling heating. The temperature measured at a height of 1.7 m represents the lowest value for UH and the highest

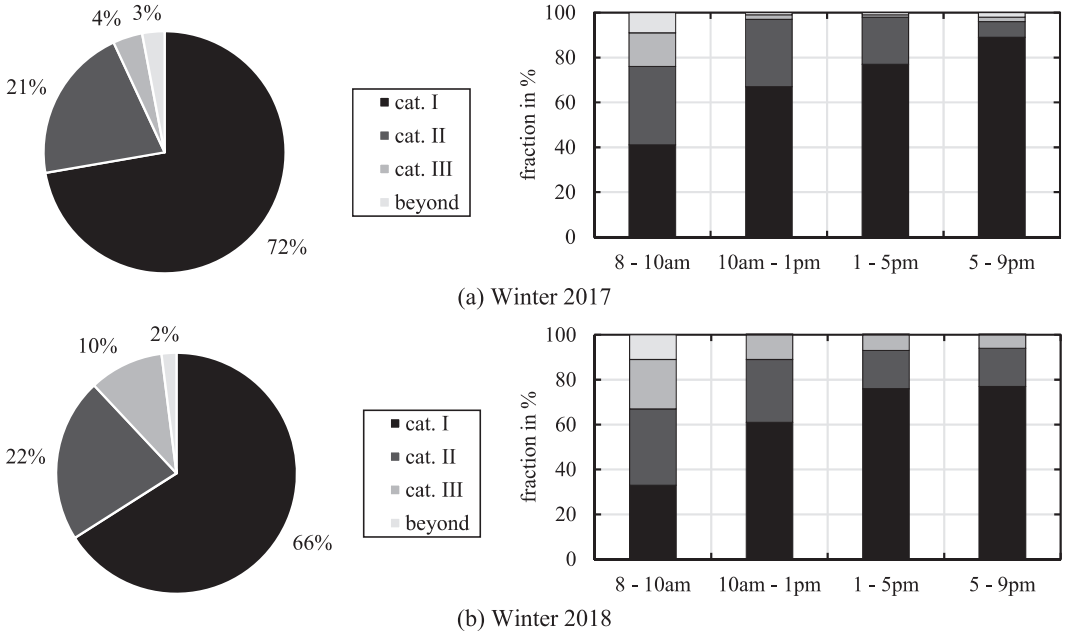

Fig. 10. Thermal comfort within the reference room during occupancy time in terms of overall comfort distribution (left) and avaraged daily comfort distribution (right) for the investigated periods.

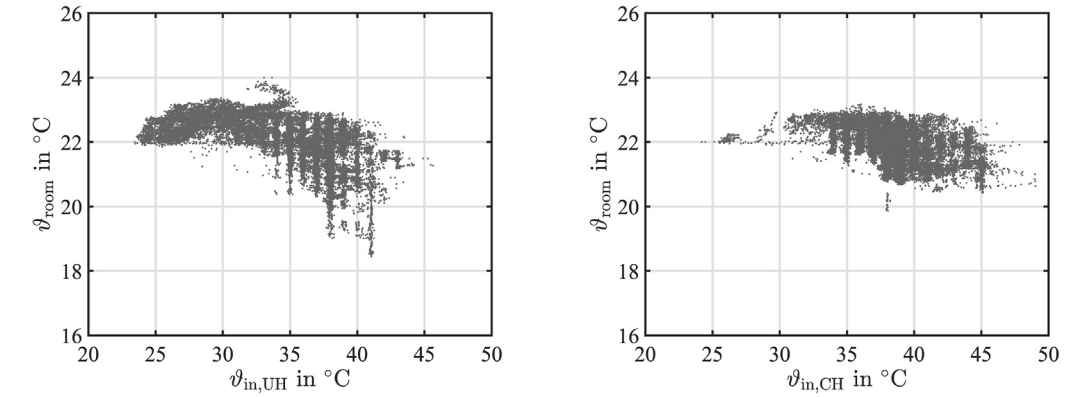

(a) Space heating with underfloor heating, winter 2017 (b) Space heating with ceiling heating, winter 2018

Fig. 11. Correlation between room temperature and surface heating inlet temperature for the investigated space heating systems.

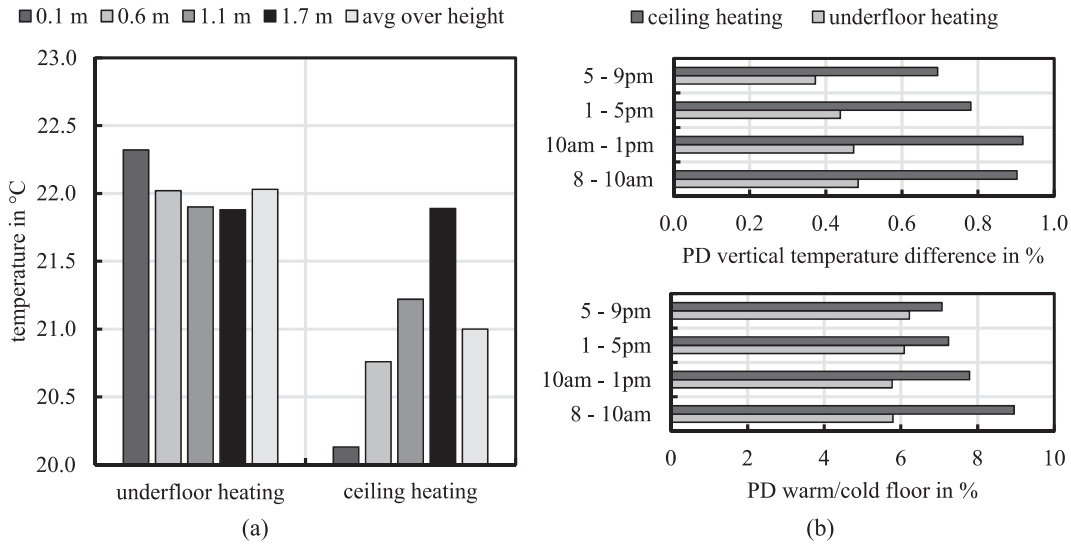

Fig. 12. Room temperatures at different heights above the floor (a) and PD values in terms of vertical temperature difference and warm/cold floor (b) for the investigated space heating systems.

value achieved for CH. While the temperature difference $\Delta\vartheta_{1-4,UH}$ was in the range of measurement uncertainty using UH, this temperature difference was $\Delta\vartheta_{1-4,CH} = 1.8$ K using CH. These results confirm the thermodynamic advantages of UH for space heating. In order to quantify the effects of the presented differences on thermal comfort, the local thermal discomfort with regard to vertical temperature and floor surface temperature are plotted in the diagrams of Fig. 12(b) following the procedure in Ref. [23]. As already shown in Fig. 10, the results averaged over the entire winter period were also broken down into time of day. The bar plots show the results for the percentage of dissatisfied (PD) in terms of the vertical temperature difference and a warm/cold floor surface. Even if UH achieved better results in terms of both comfort criteria, the values are still below the limits for local discomfort according to cat. I.

4. System simulation

The system simulation is based on the system model presented in Ref. [21]. All component models as well as the system model have been developed using the object-oriented and equation-based modeling language Modelica.

4.1. Component models

As enthalpy transfer within the AHU is a key function of the considered system in winter mode, the modeling approaches for the investigated desiccant materials are presented in the following. For this study, a detailed model of the desiccant wheel as presented in Refs. [26,27] was validated for winter operation mode. With constant ambient conditions, a dynamic equilibrium between sorption and desorption is established on the sorbent surface, in that as many molecules are sorbed as are desorbed. This sorption equilibrium can, for example, be represented with the help of isotherms as a function of the sorbent load on relative humidity. The corresponding isotherm for LiCl with respect to winter mode was developed by Gazinski and Szczechowiak [28]. The correlation is given in Equation (5).

$$\ln \phi_{eq,LiCl} = -\left(\frac{q_{LiCl}}{f_1(\vartheta)}\right)^{f_2(\vartheta)} \tag{5}$$

The coefficients are $f_1(\vartheta) = -2.0639 \cdot 10^2 \cdot \vartheta + 2.832291$ and $f_2(\vartheta) = -3.3 \cdot 10^3 \cdot \vartheta - 1.207195$, and the equilibrium humidity ratio is defined as $q_{LiCl} = m_w/m_{LiCl}$. The adsorption isotherm for

SiO_2, as developed by Pesaran and Mills [29], is provided in Equation (6).

$$\phi_{eq,SiO_2} = 0.0078 - 0.076 \cdot q_{SiO_2} + 24.2 \cdot q_{SiO_2}^2 - 124 \cdot q_{SiO_2}^3 + 204 \cdot q_{SiO_2}^4 \quad (6)$$

The equilibrium humidity ratio is defined as $q_{SiO_2} = m_w / m_{SiO_2}$. The physical based models (ph) were validated using measurement data from the test facility. For system simulations, simplified models are preferable due to shorter computing time. These efficiency models (eff) are based on simple functional relationships that describe the calculation of the output parameters from the input parameters. The required parameters were estimated using measurement data. A variant of this model approach is the effectiveness method, according to which the models of the desiccant wheel in dehumidification and enthalpy recovery mode were built. Since both heat and mass transfer take place in the desiccant wheel, two efficiencies or key figures have to be defined in order to be able to clearly describe the state change of the process air. A pair of key figures is recommended, which is described in more detail in the studies of Ruivo et al. [30–32]. These are the efficiency η_q and the key figure η_h.

$$\eta_q = \frac{q_{pro,out} - q_{pro,in}}{q_{eta,in} - q_{pro,in}}, \quad \eta_h = \frac{h_{pro,out} - h_{pro,in}}{h_{eta,in} - h_{pro,in}} \quad (7)$$

The efficiency η_q describes the efficiency of the (de)humidification process. For ideal mass transfer, η_q assumes a value of 1 in steady state. In case of an ideal, isenthalpic, state change of process air in dehumidification mode, the key figure η_h assumes a value of almost 0, while in winter operation a value of almost 1 is aimed for η_h for enthalpy recovery. Using the effectiveness parameters provided in Table 6, the process air outlet conditions of the enthalpy wheels $q_{pro,out}$ and $h_{pro,out}$ can be calculated with sufficient accuracy.

Validation plots for air temperature and humidity ratio with regard to the outside and process air outlet conditions are shown in Fig. 11 for the desiccant materials investigated. These validation results are based on chosen periods with dynamic plant operation in moisture recovery mode.

The simulated outlet temperature and humidity ratio of the process air show a good agreement with the corresponding measured values, especially for LiCl. With regard to Fig. 13(a), the differences between the results of the physical model and the efficiency model are very small. For the period under consideration, the mean deviation between the simulated outlet temperature of the process air in the efficiency model and that in the physical model is + 0.05 K. The corresponding humidity ratio is simulated on average by $-0.12 g_w/kg_{air}$ less than in the physical model. These deviations are smaller than the uncertainties of the measured values. The deviations between the physical model and the associated measured values are of the same order of magnitude. Startup effects have to be excluded from this presentation. A slightly different situation exists when modeling the enthalpy recovery with SiO_2, see Fig. 11(b). The differences between the physical modeling and the associated measured values appear more clearly than the differences between the results of the efficiency modeling and the reference values. This is largely due to the fact that not all of the material properties required for physical modeling were available for SiO_2. The mean deviations between the physical model and the measured values for the temperature are −2.7 K and for the humidity ratio $-0.4 g_w/kg_{air}$. This means that there is an extended relative temperature deviation of 13.5% for the validation, which is defined as permissible. A permissible limit of ±10 % was observed for the humidity ratio. The main causes of the deviations are the implemented equations for the sorption isotherm and the sorption enthalpy, for which no information from the wheel manufacturer was available. The material properties taken from Ref. [29] generally provide a good match of the results. The deviations between the efficiency model and the measured values are on average at + 0.2 K or $+0.1 g_w/kg_{air}$ and are therefore in the range of measurement uncertainty.

Fig. 14 shows a material comparison between LiCl and SiO_2 for different outside and indoor air conditions based on the physical models. The different outside air conditions are listed in Table 7, whereas room conditions were set to $\vartheta_{ida1} = 20\ °C$, $x_{ida1} = 5 g_w/kg_{air}$ and $\vartheta_{ida\,2} = 24\ °C$, $x_{ida2} = 7 g_w/kg_{air}$. The rotational speed was set equal for both materials at $\omega =$ 240 rph.

The moisture recovery efficiency was highest using SiO_2 for most operating points and moisture uptake was higher at the same time compared with LiCl. But heat recovery efficiency was similar for both materials for the entire range of the boundary conditions investigated. The average moisture recovery efficiencies for both materials are $\overline{\Psi}_{SiO_2} = 0.75$ and $\overline{\Psi}_{LiCl} = 0.72$. Considering boundary conditions as a combination of x_{oda2} and room conditions of ida 1, both materials show poor moisture recovery performance due to the insufficient moisture potential. The temperature dependence of efficiency was more evident for LiCl. To improve the moisture recovery efficiency of LiCl, higher rotational speed (ω) is required. Generally, Ψ_{LiCl} shows a stronger dependency on ω. Further numerical studies revealed that efficiencies close to that of SiO_2 are possible at higher rotational speeds ($\omega > 300$ rph).

Table 6
Effectiveness parameters for desiccant wheels in enthalpy recovery mode.

Desiccant material	η_q	η_h
LiCl	$0.0193 \cdot (q_{pro,in} - q_{pro,out}) + 0.8241$	0.72
SiO_2	0.86	0.83

4.2. System simulation models

Without going into the details of further component models and the implemented operation strategy, some results of the system simulation are briefly discussed below. TMY 3 weather data have been used for the location of Hamburg, Germany, January till March. Three configurations of the investigated system were simulated. With regard to Fig. 15, system configuration EW-GEO I complies with the experimentally investigated system for 2017 as the reference process, relying on a modulating GCHP system as the investigated system. The other configurations EW-GEO II and EW-GEO III have different GCHP systems and do not use a CHP as backup system. The model of EW-GEO II uses the same GCHP system as EW-GEO I but in monovalent operation at maximum power output without night shutdown and EW-GEO III is relying on a more efficient and more powerful GCHP system ($COP_{GCHP,III,max} = 4.6$, $\dot{Q}_{GCHP,III,max} = 6.4\ kW_{th}$ at BW0 /W35) in monovalent operation. The objectives are to analyze the need for a backup system, to increase the geothermal assisted heat supply and to improve environmental compatibility of the system. The comparison in Fig. 15(a) shows that the backup system can be avoided regarding the amount of final energy for heating purposes. Whereas the GCHP cover ratio was obtained to be 39.8% for the reference process (EW-GEO I), this was increased to 90% for the comparative systems (EW-GEO II/III). The main difference between the systems EW-GEO II and EW-GEO III is the relationship between thermal energy output ($Q_{GCHP,con}$) and electrical energy demand

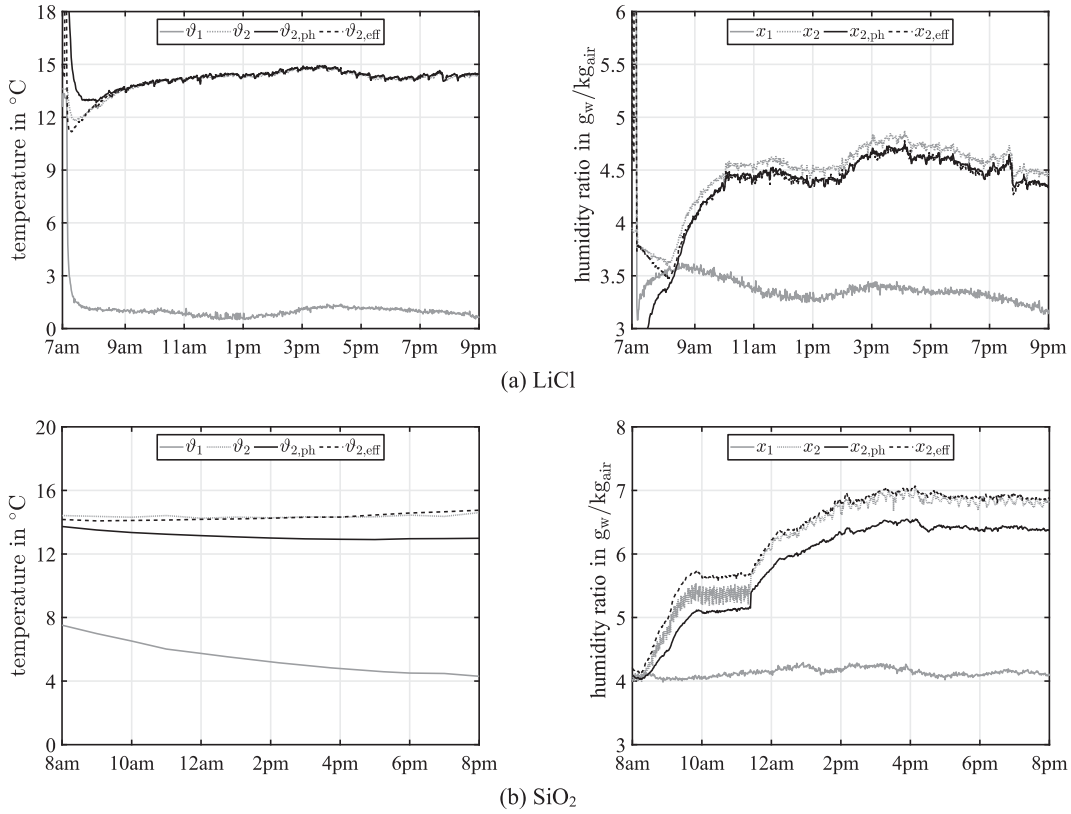

Fig. 13. Comparison between measurement results and the corresponding simulation output results of the physically based wheel model and the efficiency model for the desiccant materials examined.

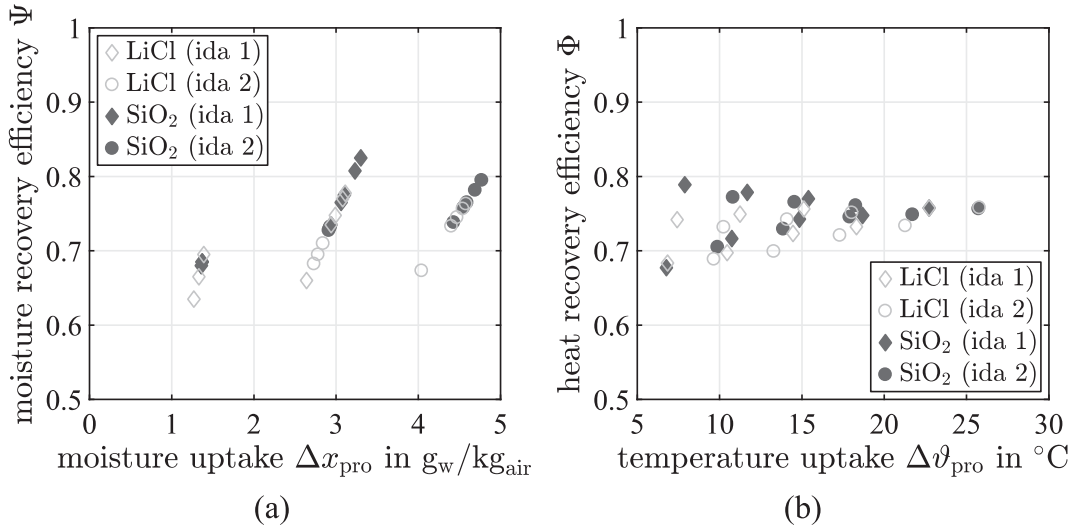

Fig. 14. Numerical performance comparison of desiccant materials in terms of moisture recovery efficiency (a) and heat recovery efficiency (b) for different air conditions.

Table 7
Outside air conditions for desiccant comparison.

$\vartheta_{oda1,2}$ in °C	x_{oda1} in g_w/kg_{air}	x_{oda2} in g_w/kg_{air}
10	1	3
5	1	3
0	1	3
−5	1	–
−10	1	–

(W_{GCHP}) of the GCHP process with improved performance for system EW-GEO III. In addition, the original GCHP system runs in inconvenient operation conditions due to the changed operating strategy for system EW-GEO II compared with EW-GEO I. These inconvenient operation conditions are a result of the performance characteristic of the GCHP used and the fact that the GCHP system is operated at maximum compressor power and low evaporator inlet temperatures. The resulting seasonal performance factors for all three GCHP systems were calculated using Equation (8).

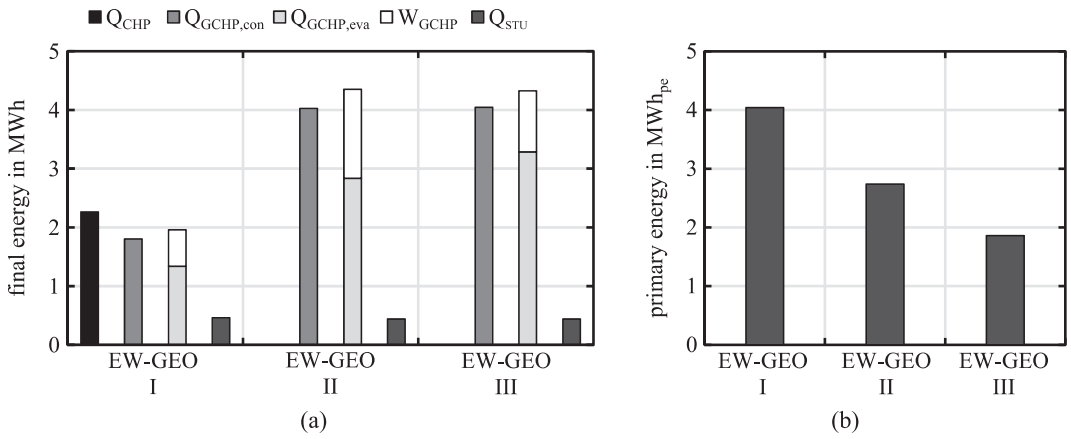

Fig. 15. Final energy supply/demand (a) and primary energy demand (b) of heat supply for different simulated system configuration.

$$SPF_{GCHP} = \frac{\int \dot{Q}_{GCHP,h}\, d\tau}{\int (P_{GCHP} + P_{AUX}) d\tau} \quad (8)$$

The simulation results with regard to GCHP performance during the period considered are $SPF_{GCHP,\ I} = 2.91$, $SPF_{GCHP,\ II} = 2.65$ and $SPF_{GCHP,\ III} = 3.98$. The effects on the resulting non-renewable primary energy demand for heat supply are presented in Fig. 15(b). The non-renewable primary energy factors for natural gas (CHP) and electricity (GCHP, AUX) are $f_{pe,gas} = 1.1$ and $f_{pe,el} = 1.8$ according to DIN V 18,599–1 [33]. EW-GEO I corresponds to a primary energy equivalent of 4.04 MWh. For the modified system configurations, reductions in primary energy demand of 32% (EW-GEO II) and 54% (EW-GEO III) were achieved.

In contrast to the system EW-GEO I, in the other simulated system configurations (EW-GEO II & III) energy in the form of heat is provide only by the GCHP system and the STU. As a result, the required heat supply by the GCHP is increased and more thermal energy is extracted from the soil. However, excessive soil cooling should be avoided in order to not impair the functioning of the geothermal system. To investigate this, simulations were carried out for the system configurations with monovalent GCHP system.

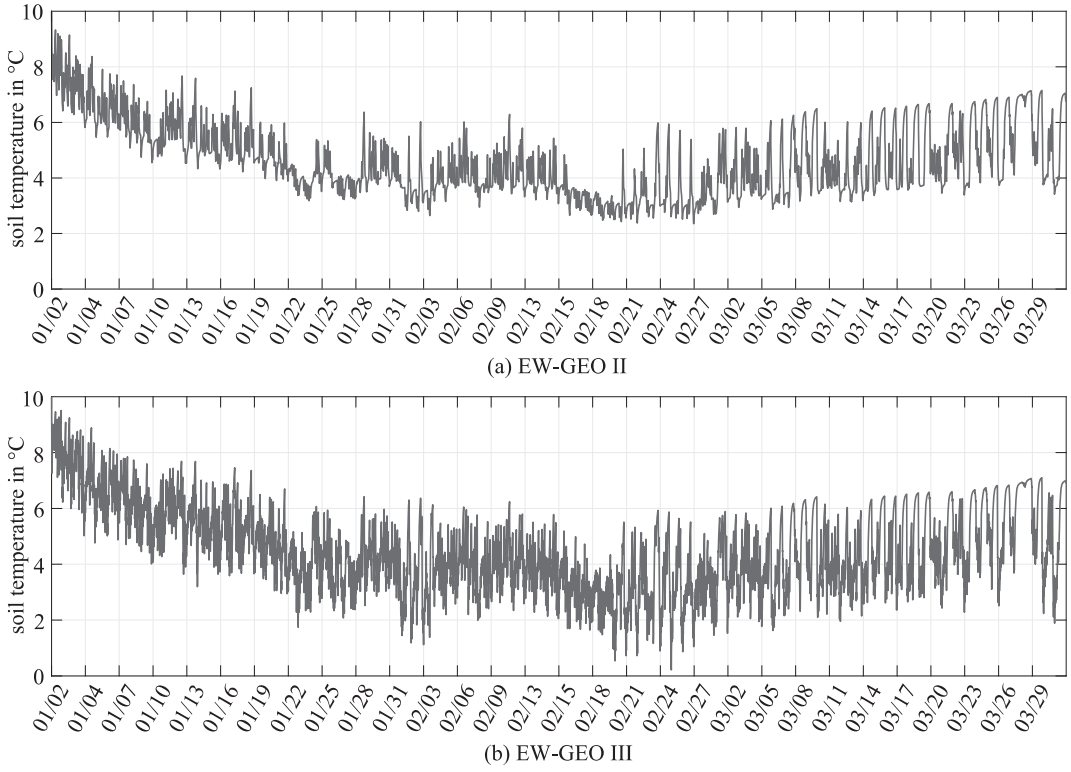

Fig. 16. Soil temperatures for the simulated system configuration with monovalent GCHP operation, (a) EW-GEO II and (b) EW-GEO III, for the considered winter period.

The curves of the resulting temperature of the soil are shown in Fig. 16. The soil temperatures shown are averaged over the temperatures in the depths of 20, 40, 60 and 80 m.

For system EW-GEO II with the existing GCHP in monovalent operation, the lowest temperature during the simulated winter period from January till March was 2.6 °C. During the same period, lower values of the mean soil temperature just above freezing were reached for system EW-GEO III with a more efficient GCHP system. Summarizing, the mean temperatures of the soil for both system configurations were always above 0 °C. As a result, there was no risk of freezing ground water. Thus, monovalent GCHP operation without night shutdown was permissible according to Ref. [34] under the boundary conditions present in the simulation.

5. Conclusions

In this study experimental and numerical investigations of an air conditioning system relying on moisture recovery and geothermal assisted heat supply are presented. Different system configurations were considered. Against the background of dry indoor air conditions, different desiccant materials were tested in terms of enthalpy recovery. The investigations showed beneficial system operation using SiO_2 compared with LiCl. Based on measurement data, an average moisture recovery efficiency of 0.83 was achieved for SiO_2. The improved heat recovery efficiency of the SiO_2-wheel lead to an average reduction of 76.1% in daily reheating demand. However, thermal comfort was maintained on a high level using UH or CH. The requirements for comfort category II were met for at least 88% of time. Furthermore, enthalpy recovery as well as system operation were investigated numerically using Modelica. With the help of physical based component simulations it is obtained that SiO_2 is beneficial against other materials for most temperate climate conditions. A system simulation model was used to investigate multiple system configurations. The simulation results show that a backup system can be avoided, reducing the primary energy demand for heat supply by up to 54%. In future investigations, full-year system performance will be considered for different locations.

Credit author statement

Peter Niemann: Conceptualization, Methodology, Software, Validation, Formal analysis, Investigation, Data curation, Writing - original draft, Writing - review & editing, Visualization, Project administration. Gerhard Schmitz: Conceptualization, Validation, Resources, Supervision, Project administration, Funding acquisition.

Declaration of competing interest

The authors declare that they have no known competing financial interests or personal relationships that could have appeared to influence the work reported in this paper.

Acknowledgement

This work is being conducted in the frame of a project funded by the German Federal Ministry for Economic Affairs and Energy (www.bmwi.de), cf. project funding reference number 03ET1421A.

Nomenclature

Symbols

A	area (m^2)
COP	coefficient of performance (−)
d	diameter (m)
f	coefficient (−)
f_{pe}	primary energy factor (−)
h	specific enthalpy (J/kg_{air})
k	heat transition coefficient ($W/(m^2K)$)
m	mass (kg)
p	pressure (Pa)
P	electrical power (W)
PD	percentage of dissatisfied (%)
q	desiccant humidity ratio ($kg_w/kg_{desiccant}$)
Q	thermal energy (kWh_{th})
$\dot{Q}$	heat flux (W)
SPF	seasonal performance factor (−)
$\dot{V}$	volumetric flow rate (m^3/h)
W	electrical energy (kWh_{el})
x	humidity ratio (kg_w/kg_{air})
z	depth (m)
α	cover ratio (−)
Δ	difference (−)
η	effectiveness parameter (−)
ϑ	temperature (°C)
v_a	air velocity (m/s)
τ	time (s)
Φ	heat recovery efficiency (−)
ϕ	relative humidity (% RH)
Ψ	moisture recovery efficiency (−)
ω	rotational speed (rph)
$\overline{[\ldots]}$	averaged quantity (−)

Subscripts and Abbreviations

AHU	air handling unit
AUX	auxiliary energy
BHE	borehole heat exchanger
BW0/W35	working point GCHP: brine water at 0 °C and heat output at 35 °C
cat	comfort category
CH	ceiling heating
CHP	combined heat/power generation
d	daily
eff	efficiency model
el	electrical
eq	equilibrium
eta	extract air
EW	enthalpy wheel
exa	exhaust air
GCHP	ground-coupled heat pump
h	heating
HRW	heat recovery wheel
ida	indoor air
in	inlet
LiCl	lithium chloride
lim	limit
max	maximum
min	minimum
oda	outside air
out	outlet
ph	physical based model
pro	process air
SiO_2	silica gel
STU	solar thermal unit
sup	supply air
th	thermal
UH	underfloor heating
w	water

References

[1] Davis LW, Gertler PJ. Contribution of air conditioning adoption to future energy use under global warming. Natl Acad Sci 2015;112(19):5962–7. https://doi.org/10.1073/pnas.1423558112.

[2] International Energy Agency. The future of cooling – opportunities for energy-efficient air conditioning. 2018. https://webstore.iea.org/the-future-of-cooling. [Accessed 4 June 2020].

[3] International Energy Agency. Energy technology perspectives 2015 – Scenarios & strategies to 2050, https://webstore.iea.org/energy-technology-perspectives-2015; 2015 [accessed 4 June 2020].

[4] Isaac M, Van Vuuren DP. Modeling global residential sector energy demand for heating and air conditioning in the context of climate change. Energy Pol 2009;37:507–21. https://doi.org/10.1016/j.enpol.2008.09.051.

[5] Pérez-Lombard L, Ortiz J, Pout C. A review on buildings energy consumption information. Energy Build 2008;40(3):394–8. https://doi.org/10.1016/j.enbuild.2007.03.007.

[6] Jani DB, Mishra M, Sahoo PK. Solid desiccant air conditioning – a state of the art review. Renew Sustain Energy Rev 2016;60:1451–69. https://doi.org/10.1016/j.rser.2016.03.031.

[7] Kojok F, Fardoun F, Younes R, Outbib R. Hybrid cooling systems: a review and an optimized selection scheme. Renew Sustain Energy Rev 2016;65:57–80. https://doi.org/10.1016/j.rser.2016.06.092.

[8] Bareschino P, Pepe F, Roselli C, Sasso M, Tariello F. Desiccant-based air handling unit alternatively equipped with three hygroscopic materials and driven by solar energy. Energies 2019;12(8):1543. https://doi.org/10.3390/en12081543.

[9] De Antonellis S, Intini M, Joppolo CM, Molinaroli L, Romano F. Desiccant wheels for air humidification: an experimental and numerical analysis. Energy Convers Manag 2015;106:355–64. https://doi.org/10.1016/j.enconman.2015.09.034.

[10] La D, Dai Y, Li H, Li Y, Kiplagat JK, Wang R. Experimental investigation and theoretical analysis of solar heating and humidification system with desiccant rotor. Energy Build 2011;43:1113–22. https://doi.org/10.1016/j.enbuild.2010.08.006.

[11] Kawamoto K, Cho W, Kohno H, Koganei M, Ooka R, Kata S. Field study on humidification performance of desiccant air-conditioning system combined with a heat pump. Energies 2016;9(2):89. https://doi.org/10.3390/en9020089.

[12] Kashif A, Ali M, Sheikh NA, Vukovic V, Shehryar M. Experimental analysis of a solar assisted desiccant-based space heating and humidification system for cold and dry climates. Appl Therm Eng 2020;175:115371. https://doi.org/10.1016/j.applthermaleng.2020.115371.

[13] Preisler A, Brychta M. High potential of full year operation with solar driven desiccant evaporative cooling systems. Energy Procedia 2012;30:668–75. https://doi.org/10.1016/j.egypro.2012.11.076.

[14] Niemann P, Schmitz G. Experimental investigation of a ground-coupled air conditioning system with desiccant assisted enthalpy recovery during winter mode. Appl Therm Eng 2019;160:114017. https://doi.org/10.1016/j.applthermaleng.2019.114017.

[15] Niemann P, Richter F, Speerforck A, Schmitz G. Desiccant-assisted air conditioning system relying on solar and geothermal energy during summer and winter. Energies 2019;12(16):3175. https://doi.org/10.3390/en12163175.

[16] Zhao Y, Sun H, Tu D. Effect of mechanical ventilation and natural ventilation on indoor climates in Urumqi residential buildings. Build Environ 2018;144:108–18. https://doi.org/10.1016/j.buildenv.2018.08.021.

[17] Yang W, Marr LC. Dynamics of airborne influenza A viruses indoors and dependence on humidity. PloS One 2011;6(6):e21481. https://doi.org/10.1371/journal.pone.0021481.

[18] Noti JD, Blachere FM, McMillen CM, Lindsley WG, Kashon ML, Slaughter DR, Beezhold DH. High humidity leads to loss of infectious influenza virus from simulated coughs. PloS One 2013;8(2):e57485. https://doi.org/10.1371/journal.pone.0057485.

[19] Rafique MM, Gandhidasan P, Bahaidarah HMS. Liquid desiccant materials and dehumidifiers – a review. Renew Sustain Energy Rev 2016;56:179–95. https://doi.org/10.1016/j.rser.2015.11.061.

[20] Li Z, Li D. Study on the dehumidification and indoor air cleaning performance of rotary desiccant rotor. Procedia Eng 2017;205:497–502. https://doi.org/10.1016/j.proeng.2017.10.402.

[21] Speerforck A. Investigation of a desiccant assisted geothermal air conditioning system. first ed. Munich, Germany: Verlag Dr. Hut; 2019.

[22] DIN EN ISO 7726. Ergonomics of the thermal environment – instruments for measuring physical quantities. Berlin, Germany: Beuth; 2002 (ISO 7726: 1998); German version EN ISO 7726: 2001.

[23] DIN EN ISO 7730. Ergonomics of the thermal environment – analytical determination and interpretation of thermal comfort using calculation of the PMV and PPD indices and local thermal comfort criteria. Berlin, Germany: Beuth; 2006 (ISO 7730: 2005); German version EN ISO 7730: 2005.

[24] Kottek M, Grieser J, Beck C, Rudolf B, Rubel F. World map of the Köppen-Geiger climate classification update. Meteorol Z 2006;15(3):259–63. https://doi.org/10.1127/0941-2948/2006/0130.

[25] DIN EN 15251. Indoor environmental input for design and assessment of energy performance in buildings addressing indoor air quality, thermal environment, lighting and acoustics. Berlin, Germany: Beuth; 2007.

[26] Casas W. Untersuchung und Optimierung sorptionsgestützter Klimatisierungsprozesse. first ed. Göttingen, Germany: Cuvillier Verlag; 2005.

[27] Wrobel J, Morgenstern P, Schmitz G. Modeling and experimental validation of the desiccant wheel in a hybrid desiccant air conditioning system. Appl Therm Eng 2013;51:1082–91. https://doi.org/10.1016/j.applthermaleng.2012.09.033.

[28] Gazinski B, Szczechiowiak E. Die thermodynamischen Grundlagen der Luftentfeuchtung mit Hilfe der wässrigen Lithiumbromid- und Lithiumchlorid-Lösungen. KI Klima-Kälte-Heizung 1984;12(1):509–15.

[29] Pesaran AA, Mills AF. Moisture transport in silica gel packed beds – ii. Experimental study. Int J Heat Mass Tran 1987;30(6):1051–60.

[30] Ruivo CR, Costa JJ, Figueiredo AR, Kodama A. Effectiveness parameters for the prediction of the global performance of desiccant wheels – an assessment based on experimental data. Renew Energy 2012;38:181–7. https://doi.org/10.1016/j.renene.2011.07.023.

[31] Ruivo CR, Carillo-Andrés A, Costa JJ, Domínguez-Muñoz F. A new approach to the effectiveness method for the simulation of desiccant wheels with variable inlet states and airflow rates. Appl Therm Eng 2013;58:670–8. https://doi.org/10.1016/j.applthermaleng.2011.12.052.

[32] Ruivo CR, Carillo-Andrés A, Costa JJ, Domínguez-Muñoz F. Exponential correlations to predict the dependence of effectiveness parameters of a desiccant wheel on the airflow rates and on the rotational speed. Appl Therm Eng 2013;51:442–50. https://doi.org/10.1016/j.applthermaleng.2012.08.037.

[33] DIN V 18599-1. Energy efficiency of buildings – calculation of the net, final and primary energy demand for heating, cooling, ventilation, domestic hot water and lighting – Part 1. Berlin, Germany: Beuth; 2018.

[34] VDI 4640. Thermal use of the underground – ground source heat pump systems; Part 2. Berlin, Germany: Beuth; 2019.